Periodic-phase acoustic vortices with tunable comb-like orbital angular momentum spectrum

Xin-Rui Li, Jia-Jia Feng, Bu-Chen Ping, Yang Sun, Da-Jian Wu, Badreddine Assouar

Periodic-phase acoustic vortices with tunable comb-like orbital angular momentum spectrum

Xin-Rui Li,[1] Jia-Jia Feng,[1] Bu-Chen Ping,[1] Yang Sun,[1] Da-Jian Wu,[1,*] and Badreddine Assouar[2,†]

[1] *Jiangsu Key Lab of Opto-Electronic Technology, School of Physics and Technology, Nanjing Normal University, Nanjing 210023, China*

[2] *Université de Lorraine, CNRS, Institut Jean Lamour, Nancy 54000, France*

Acoustic vortices (AVs) carrying orbital angular momentum (OAM) have shown great significance in communication. However, the crosstalk in the acoustic communication based on traditional AV with single OAM remains an issue. Here, we propose a periodic-phase acoustic vortex (PPAV) with comb-like OAM spectrum. The sample interval of OAM spectrum of the PPAV can be modulated by the period number of the azimuthal phase. The influence of the period number on the acoustic properties of the PPAV and the evolution of the PPAV are investigated in theoretical analysis. Moreover, an acoustic artificial structure plate engraved with 24 filled circular holes is designed to generate the PPAVs in water. By changing the height of the resin layer filled in each hole unit, the transmitted phase shift of the ultrasonic wave through them could be flexibly and efficiently manipulated. Both simulations and experiment confirm that the designed artificial plate with filled holes can produce the PPAV with arbitrary topological charge. Finally, we have preliminarily explored the possibility of applying the PPAV in acoustic communication and show that the OAM sample interval of the PPAV could be used as an independent degree of freedom for acoustic encoding/decoding communication. We believe that the PPAVs generated by the acoustic artificial structure plates may find good applications in microparticle manipulation and acoustic communication.

[*] wudajian@njnu.edu.cn

[†] badreddine.assouar@univ-lorraine.fr

I. INTRODUCTION

Orbital angular momentum (OAM), one of basic physical natures of acoustic vortex (AV), has gained increasing interests due to its unique applications in microparticle manipulation and acoustic communication [1-9]. Theoretically, the communication capacity of the OAM beam can be increased infinitely due to the orthogonality of OAMs with different modes [10-13]. On this account, a series of investigations concentrate on the OAM multiplexing and demultiplexing in acoustic communication, which was demonstrated to be able to greatly increase the information capacity. In communications, crosstalk is a crucial problem that causes disruptions within the process of date transmission and it is inevitable [14-16]. The crosstalk between orthogonal bases is an important index to verify the accuracy and robustness of an acoustic communication system, and greater crosstalk between orthogonal bases will result in a degradation of the signals that are received [4,17]. Therefore, it is highly desirable to construct acoustic communications with minimal channel crosstalk [18]. The conventional integer AVs have a single OAM that is merely determined by the topological charge (TC) [14,19]. Many investigations have shown that the energy of transmitted single OAM mode will be leaked into the neighboring OAM modes and other channels [16,20,21], and hence the expectation information at the receiver end does not match with the measured transmitted modes [15]. Recently, it was reported that the optical vortex (OV) carrying more OAM modes is beneficial to reduce the mode crosstalk [22,23] and increase the robustness [24]. Accordingly, many OVs with more OAM modes and tailorable OAM spectra have been proposed and investigated [25-29]. In this context, OAM multiformity of the AV also could help to improve the communication quality.

Ultrasonic waves are dominant carrier of underwater communications because of the rapid decay of light and electromagnetic waves [2,14,30] in such a medium. Acoustic artificial metamaterials have received a lot of attention recently in ultrasonic research [31-33], opening

up a novel path for the manipulation of ultrasonic waves. Furthermore, considerable efforts have been devoted to the investigations on the generation of ultrasonic AV and its underwater applications, especially in acoustic communications [2,3,34,35]. The general method for generating the ultrasonic AV is based on the transducer array that can flexibly modulate the generation of the ultrasonic AV [3]. The passive method based on the artificial structure plate (ASP) is another choice, and it has attracted great attention due to its superiority of simplicity, economy, and ease of miniaturization. Many strategies, such as multi-arm coiling slits, discrete spiral structure plates, and degenerated pinhole plates, etc. have been successfully explored to realize the ultrasonic AVs in water, which further have found applications in microparticle manipulation and acoustic communication. However, for an ultrasonic AV with a large TC or the multimode ultrasonic AV, the single spatial phase modulation cannot meet the exquisite-designed phase requirements. Hence the additional regulatory degree of freedom is needed.

In this paper, we propose a periodic-phase acoustic vortex (PPAV) with comb-like OAM spectrum. By changing the period number of the azimuthal phase, the sample interval of OAM spectrum of the PPAV can be adjusted. The normalized acoustic intensity distributions, phase distributions, and OAM spectra of the PPAV are carefully studied in theoretical analysis and numerical simulation. An acoustic artificial structure plate (AASP) engraved with 24 filled circular holes (CHs) is designed to achieve the PPAVs in water. By changing the height of the resin layer filled in each hole unit, the transmitted phase shift of the ultrasonic wave through them could be flexibly and efficiently manipulated. Hence, the PPAVs with arbitrary TCs and OAM sample interval can be achieved. The further experiment confirms that the proposed AASP could generate PPAV. Finally, we illustrate the possibility of acoustic encoding/decoding communication based on the OAM sample interval of the PPAV.

II. THEORETICAL ANALYSIS

To better introduce the proposed concept of PPAV, we have started from the definition of the conventional acoustic vortex (CAV). The acoustic field of CAV can be expressed as [4]

$$P_{\mathrm{CAV}}\left(r,\theta\right)=P_0\exp\left(i\psi_{\mathrm{CAV}}\right), \tag{1}$$

where P_0 is the amplitude, the phase of the CAV is $\psi_{\mathrm{CAV}}=m\theta$, m means the topological charge (TC), and the azimuthal angle θ increases from 0 to 2π. Similar to the CAV [4], the acoustic field of the proposed PPAV can be written as

$$P_{\mathrm{PPAV}}\left(r,\theta\right)=P_0\exp\left(i\psi_{\mathrm{PPAV}}\right), \tag{2}$$

where P_0 and ψ_{PPAV} are the amplitude and phase of the PPAV, respectively. The phase of the PPAV ψ_{PPAV} is divided into N periods as the azimuthal angle θ increases from 0 to 2π. The phase shift in each period is $2\pi l/N$, where l is the TC of the PPAV. Each period consists of two piecewise phase functions, the first of which has a phase shift that is an integral multiple of 2π ($A=2\pi n$) and the second of which has a fractional phase jump ($B=2\pi l/N-2\pi n$), where $n=[l/N]$ is the phase jump factor and [.] denotes the least integer function. Therefore, the phase function of the PPAV in the first period is expressed as

$$\psi_{\mathrm{PPAV}}=\begin{cases} l\theta, & 0\le\theta<\dfrac{2\pi n}{l} \\ l\theta-2\pi n, & \dfrac{2\pi n}{l}\le\theta<\dfrac{2\pi}{N} \end{cases}. \tag{3}$$

Then, as the azimuthal angle θ increases from 0 to 2π, the phase function of the PPAV can be written as

$$\psi_{\mathrm{PPAV}}=\begin{cases} l\left(\theta-\dfrac{2\pi q}{N}\right), & \dfrac{2\pi q}{N}\le\theta<\dfrac{2\pi n}{l}+\dfrac{2\pi q}{N} \\ l\left(\theta-\dfrac{2\pi q}{N}\right)-2\pi n, & \dfrac{2\pi n}{l}+\dfrac{2\pi q}{N}\le\theta<\dfrac{2\pi\left(1+q\right)}{N} \end{cases},\quad \left(q=0,1,\ldots N-1\right). \tag{4}$$

The acoustic field of the PPAV can be expressed as

$$P_{\mathrm{PPAV}}\left(r,\theta\right)=\sum_{q=0}^{N-1}p\left(r,\theta+\frac{2\pi q}{N}\right), \tag{5}$$

where $p(r, \theta)$ denotes the acoustic field of each azimuthal phase period. It was reported that an arbitrary acoustic field can be decomposed into a set of orthonormal bases such as integer OAM states [36]. Therefore, $p(r, \theta)$ can be rewritten as [27,28]

$$p(r,\theta) = P_0 \sum_{L=-\infty}^{\infty} c_L \exp(iL\theta), \tag{6}$$

where $c_L = \left\langle \exp(iL\theta) \middle| \exp(i\psi_{\mathrm{PPAV}}) \right\rangle$ represents the expansion coefficient.

Substituting the Eq. (6) into the Eq. (5), we obtain

$$P_{\mathrm{PPAV}}(r,\theta) = P_0 \sum_{L=-\infty}^{\infty} \sum_{q=0}^{N-1} c_L \exp\left[iL\left(\theta + \frac{2\pi q}{N} \right) \right]. \tag{7}$$

The summation over q can be expressed as [36]

$$\sum_{q=0}^{N-1} \exp\left(iL \frac{2\pi q}{N} \right) = \begin{cases} N, & L = KN \\ 0, & L \neq KN \end{cases}, \tag{8}$$

where K is an integer. Then, the Eq. (7) can be rewritten as

$$P_{\mathrm{PPAV}}(r,\theta) = \begin{cases} P_0 N \sum_{L=-\infty}^{\infty} c_L \exp(iL\theta), & L = KN \\ 0, & L \neq KN \end{cases}. \tag{9}$$

Therefore, the proposed PPAV has a comb-like OAM spectrum with the sample interval of N.

III. ANALYTICAL RESULTS AND DISCUSSIONS

To realize the PPAVs, we have first designed a theoretical model that 24 acoustic sources evenly are assigned on a circle with a radius of r to generate the desired initial phase. Figure 1(a) shows the schematic diagram of an original analytical model for generating a PPAV with l = 3 and N = 2, where 24 acoustic sources are evenly placed on a circle with the radius of r. The location of the j^{th} acoustic source is defined as $(r, \theta_j, 0)$, where $\theta_j = 2\pi(j - 1)/24$ and its corresponding phase ψ_j can be calculated using Eq. (4). According to Refs. 8 and 37, the acoustic field generated by these acoustic sources can be written as

$$P(\rho,\varphi,z,t)=\exp(-i\omega t)\sum_{j=1}^{24}\frac{P_0}{R_j}\exp(ikR_j)\exp(i\psi_j), \tag{10}$$

where $R_j=\sqrt{(\rho\cos\varphi-r\cos\theta_j)^2+(\rho\sin\varphi-r\sin\theta_j)^2+z^2}$ is the distance from the j^{th} acoustic source (r, θ_j, 0) to the observation point (ρ, φ, z) [8,37].

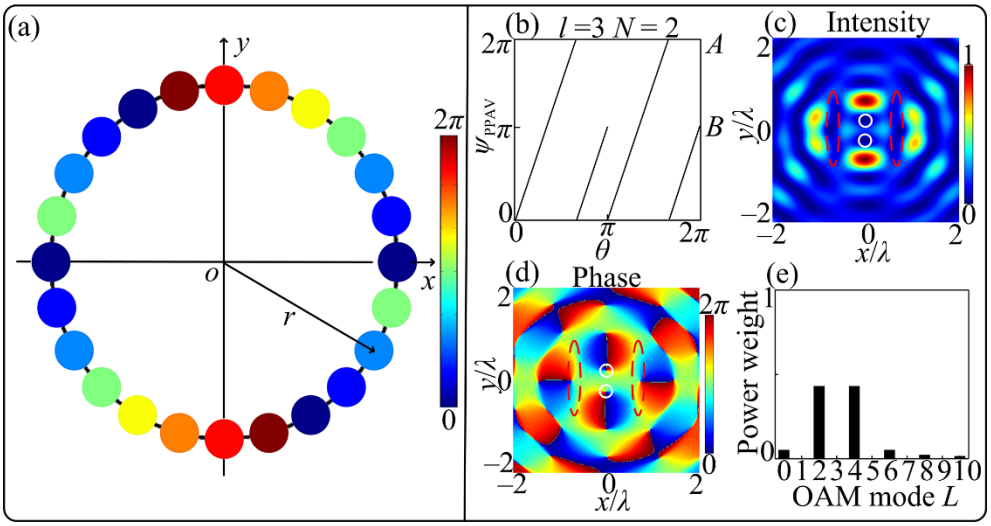

FIG. 1. (a) Schematic diagram of an original analytical model for a PPAV with TC l = 3 and period number N = 2. (b) Dependence of the phase ψ_{PPAV} of the PPAV with l = 3 and N = 2 on the azimuthal angle θ. (c) Normalized analytical acoustic intensity and (d) phase distributions of the PPAV with l = 3 and N = 2. (e) Corresponding OAM spectrum of the PPAV.

Throughout this work, the background medium is water, the incident frequency is fixed at 1 MHz, and the circle radius r is set as 14λ. Figure 1(b) shows the dependence of the phase ψ_{PPAV} of the PPAV with l = 3 and N = 2 on θ. There are two phase periods and each period provides a phase shift of [(3×2π)/2 = 3π]. As the azimuthal angle θ increases from 0 to 2π/3, the ψ_{PPAV} increases from 0 to 2π and hence A = 2π. As θ further increases from 2π/3 to π, the ψ_{PPAV} increases from 0 to π and thus B = π. In the second period of ($\pi \le \theta \le 2\pi$), the same variation of ψ_{PPAV} is observed with A = 2π and B = π. Figure 1(c) shows the normalized analytical acoustic intensity distribution of the PPAV with l = 3 and N = 2 at the plane of z = 7λ. It should be noted

that 7λ is not the limited propagation distance of the PPAVs. In the Supplement Material, we further examine the propagation characteristics of the PPAV. It has been noted that the PPAV could reach a considerable distance. There is a bright spot on the positive y-axis, while a dark one (indicated by a white solid circle) can be observed between the origin of coordinates and the bright spot. Symmetrically, another dark spot and a bright spot that can be found along the negative y-axis. Meanwhile, two bright fringes can be found on x-axis, while two dark stripes (indicated by two red dashed ellipses) between the origin and the bright fringes appear symmetrically on the positive and negative x-axis, respectively. The corresponding phase distribution is shown in Figure 1(d), where two phase singularities (indicated by two white solid circles) on y-axis corresponds to the two dark spots and two phase singularities (represented by red dashed ellipses) on x-axis corresponds to two dark stripes. In Supplementary Material, we further study the acoustic intensity and phase distributions produced by the first and second phase periods of the PPAV with $l = 3$ and $N = 2$, and confirm that a fractional phase jump of π in the first and second phase periods can make the central phase singularity splitting along the y-axis, resulting in two phase singularities on the positive and negative y-axis. Moreover, the coupling between two phase periods induces the phase singularity splitting along the x-axis, results in two phase singularities on the positive and negative x-axis. Figure 1(e) shows the OAM spectrum of the PPAV with $l = 3$ and $N = 2$. According to the Eq. (8) and Eq. (9), the superposition of OAM states is nonvanishing only when OAM component L is equal to KN. Therefore, the sample interval of the components in the OAM spectrum of the PPAV with $l = 3$ and $N = 2$ is 2. The power is mainly distributed in two OAM components of $L = 2$ and 4, and the power weights of them are both ~43.8%. In addition, there are some weak OAM modes that can be observed in Fig. 1(e). The power weights of OAM components of $L = 0$, 6, 8, and 10 are ~4.87%, ~4.87%, ~1.7%, and ~0.9%, respectively, which are in accord with the weak acoustic fields distributed at the center and the edges.

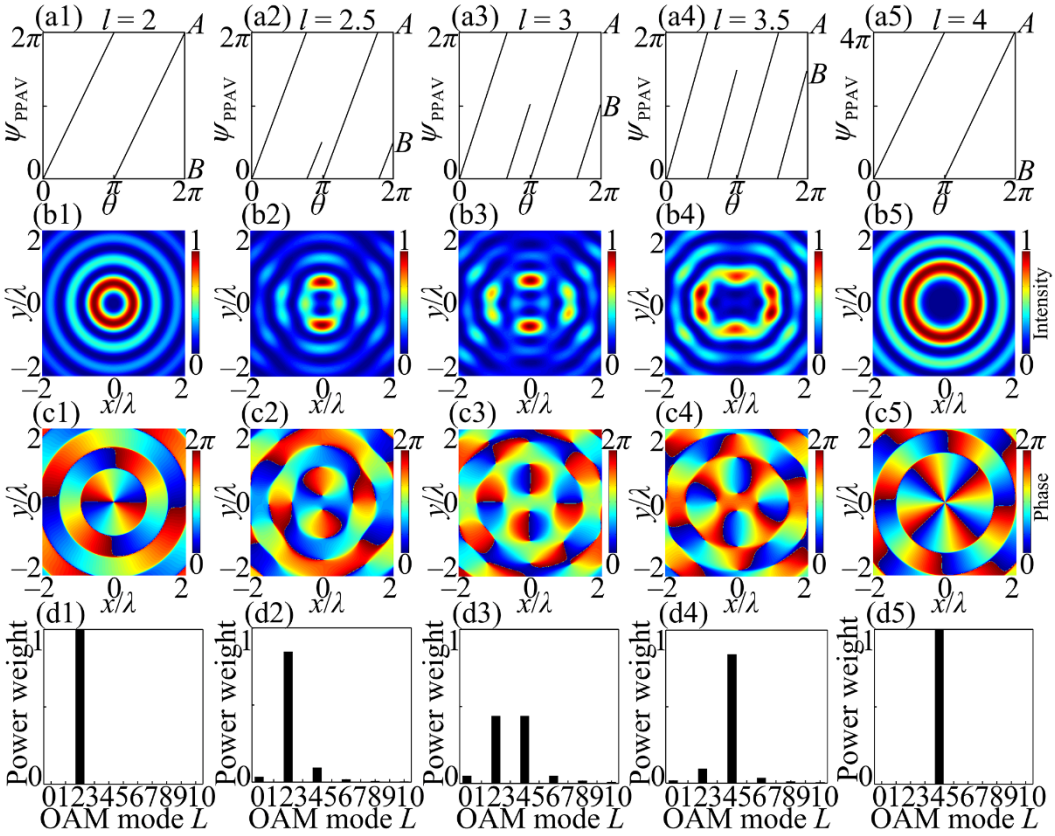

FIG. 2. (a1)-(a5) Dependencies of the phase ψ_{PPAV} of the PPAVs with l = 2, 2.5, 3, 3.5, and 4 on the azimuthal angle θ. Here, the period number N is fixed at 2. (b1)-(b5) Normalized analytical acoustic intensity and (c1)-(c5) phase distributions of the PPAVs with l = 2, 2.5, 3, 3.5, and 4. Here, the observed plane is $z = 7\lambda$. (d1)-(d5) Corresponding OAM spectra of the PPAVs.

Next, we have investigated the evolution of the PPAV with TC increasing from 2 to 4 when the period number N is fixed at 2. In Fig. 2, the first row shows the dependency of the phase ψ_{PPAV} of the PPAVs with TCs l = (a1) 2, (a2) 2.5, (a3) 3, (a4) 3.5, and (a5) 4 on θ. As N = 2, the phase shifts are $A = 2\pi$ for the PPAVs with l = 2, 2.5, 3, and 3.5, respectively, and the corresponding fractional phase jumps B = 0, 0.5π, π, and 1.5π. For the PPAV with l = 4, the phase shift A is 4π and the phase jump B is 0. The second row shows the normalized analytical acoustic intensity distributions of the PPAVs with l of (b1) 2, (b2) 2.5, (b3) 3, (b4) 3.5, and (b5)

4 at the plane of $z = 7\lambda$, while the corresponding phase distributions of the PPAVs are shown in Figs. 2(c1)-2(c5). The bottom row shows the OAM spectra of the PPAVs with l of (d1) 2, (d2) 2.5, (d3) 3, (d4) 3.5, and (d5) 4. When $l = 2$ ($A = 2\pi$ and $B = 0$), the PPAV returns to the CAV. The normalized analytical acoustic intensity distribution of the PPAV is ring-like, while the phase changes 4π along the anticlockwise direction. Moreover, the power weight of the OAM component of $L = 2$ is ~100%, as shown in Fig. 2(d1). These characteristics are consistent with those of the CAV with TC of 2. As l increases to 2.5, fractional phase jump B increases from 0 to 0.5π. The central phase singularity splits along the y-axis and hence the inner ring-like intensity pattern is broken [37], and two phase singularities on the positive and negative x-axis gradually take shape. In this case, the power weight of the OAM component of $L = 2$ decreases to ~84.5%. According to the Eq. (9), there still exist some other components in the OAM spectrum with a sample interval of 2. The power weight of OAM components of $L = 0$, 4, 6, 8, and 10 are ~3.4%, ~9%, ~1.7%, ~0.69%, and ~0.36%, respectively. As l increases to 3, the fractional phase jump B increases to π and the splitting of the phase singularity becomes maximum. The offset of two phase singularities on the positive and negative y-axis reaches a maximum, and two phase singularities on the positive and negative x-axis are fully formed. There is a bright spot on the positive y-axis, while a dark one can be observed between the origin of coordinates and the bright spot. Symmetrically, another dark spot and a bright spot can be found along the negative y-axis. Two bright fringes on x-axis are obvious, while two dark stripes between the origin of coordinates and bright fringes are fully generated. Correspondingly, the power weights of two OAM components of $L = 2$ and 4 are both ~43.8%, as shown in Fig. 2(d3). As l-value increases to 3.5, 4 phase singularities on x-axis and y-axis gradually move toward the origin, while the bright fringes on the x-axis and the bright spots on the y-axis begin to connect together and a quasi-ring with a larger radius is gradually formed. The power weight of OAM component of $L = 4$ further increases to 84% and that of $L = 2$ decreases to 9.3%.

Finally, as $l = 4$, the PPAV returns to the CAV. In this case, 4 phase singularities are completely moved to the origin, a bright ring with a larger radius is obtained, and the power weight of the OAM of $L = 4$ is ~100%. To gain insight into the evolution process of the PPAV, we carefully investigate the properties of PPAVs with TCs increasing from 2 to 4 with interval of 0.25 in Supplement Material when the period number N is fixed at 2.

On another hand, we also have investigated the influence of the period number N on the acoustic properties of the proposed PPAVs. In Fig. 3, the first row shows the variation of the ψ_{PPAV} of the PPAVs with (a1) $l = 1.5$ and $N = 1$, (a2) $l = 3$ and $N = 2$, (a3) $l = 4.5$ and $N = 3$, and (a4) $l = 6$ and $N = 4$ with the azimuthal angle θ. The phase shifts A and the phase jumps B for four PPAVs are all fixed at 2π and π, respectively. The second row represents the normalized analytical acoustic intensity distributions of the PPAVs with (b1) $l = 1.5$ and $N = 1$, (b2) $l = 3$ and $N = 2$, (b3) $l = 4.5$ and $N = 3$, and (b4) $l = 6$ and $N = 4$ at the plane of $z = 7\lambda$, while the corresponding phase profiles are shown in Figs. 3(c1)-3(c4). As seen in Figs. 3(b1) and 3(c1), two phase singularities emerge on the positive and negative y-axis, resulting in, respectively, a dark spot (indicated by a white solid circle) in the upper part of the pressure field profile and a low-intensity stripe (indicated by a red dashed ellipse) along the horizontal direction. These results match well with those of an AV with a fractional TC of 1.5 [8,37]. In this case, the PPAV returns to the AV with a TC of 1.5. It was reported that the AV with a fractional TC can be viewed as the superposition of a series of AVs with integer TCs, each one weighted with the Fourier coefficient [38]. The bottom row in Fig. 3(d1) shows the OAM spectrum of the PPAV with $l = 1.5$ and $N = 1$. The power is mainly distributed in two OAM components of $L = 1$ and 2, and the power weights of them are both ~43.2%. There are some other components with a sample interval of 1 and the power weight of OAM components of $L = 0$, 3, 4, 5, 6, 7, 8, 9 and 10 are ~4.8%, ~4.8%, ~1.7%, ~0.8%, ~0.5%, ~0.36%, ~0.3%, ~0.2%, and ~0.15%, respectively.

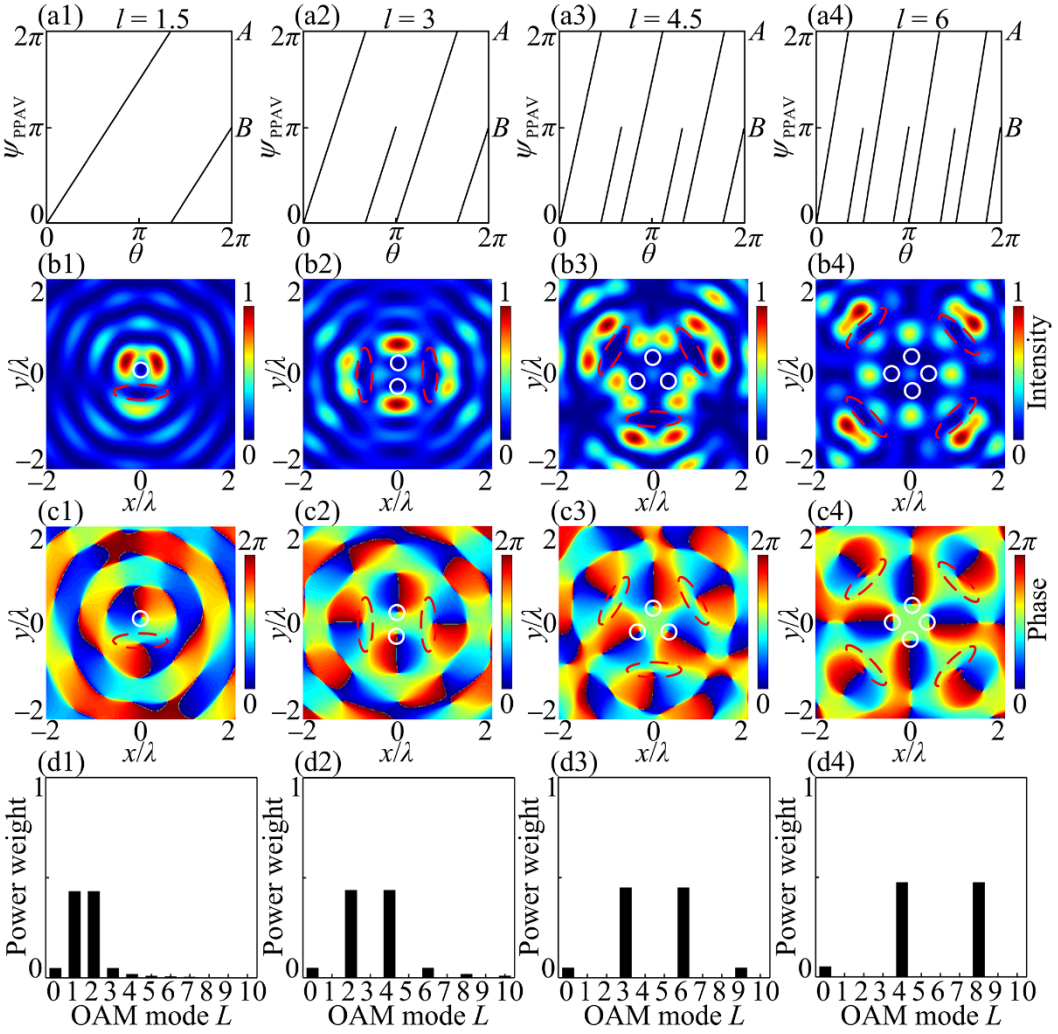

FIG. 3. Variations of the phase ψ_{PPAV} of the PPAVs with (a1) $l = 1.5$ and $N = 1$, (a2) $l = 3$ and $N = 2$, (a3) $l = 4.5$ and $N = 3$, and (a4) $l = 6$ and $N = 4$ with θ. (b1)-(b4) Normalized analytical acoustic intensity and (c1)-(c4) phase distributions of the PPAVs with $l = 1.5$ and $N = 1$, $l = 3$ and $N = 2$, $l = 4.5$ and $N = 3$, and $l = 6$ and $N = 4$. Here, the observed plane is $z = 7\lambda$. (d1)-(d4) Corresponding OAM spectra of the PPAVs.

When $l = 3$ and $N = 2$, as discussed above, the power weights of two OAM components of $L = 2$ and 4 are both ~43.8%, and the sample interval of the OAM spectrum is 2. For the PPAV with $l = 4.5$ and $N = 3$, the phase jump B of π and the period number of 3 induce the central phase singularity splitting into 3 phase singularities with a same angular interval. Meanwhile, 3 new phase singularities are formed in the outer part of the phase profile. The power weights of two

OAM components of $L = 3$ and 6 are both ~45% and the sample interval of OAM components is 3, as shown in Fig. 3(d3). When $l = 6$ and $N = 4$, as shown in Figs. 3(b4) and 3(c4), there are 4 phase singularities that split from the origin, and 4 phase singularities on the outer part of the phase distribution lead to 4 dark stripes (indicated by 4 red dashed ellipses) on the outer portion of the intensity profile. In Fig. 3(d4), the sample interval of OAM components is 4 and the power weights of two OAM components of $L = 4$ and 8 are both ~47.4%. Therefore, we have further confirmed that the sample interval of the components in the OAM spectrum of the PPAV is equal to the period number N. In Supplement Material, we also study the acoustic intensity and phase distributions of the PPAVs with same TC l but varying period number N, and further confirm that the sample interval of the components in the OAM spectrum of the PPAV is equal to the period number N.

An acoustic artificial structure plate engraved with 24 circular holes is proposed to achieve the PPAVs, as shown in Fig. 4(a). The AASP is made of stainless steel, and its thickness d_1 is fixed at 8 mm (~5.3λ). The density, longitudinal wave speed, and shear wave speed of stainless steel are 7900 kg·m^{-3}, 5240 m·s^{-1}, and 2978 m·s^{-1}, respectively, and the acoustic impedance is ~28 times that of water [6,34]. Thus, it can be used as the acoustic rigid material in water. As shown in Fig. 4(b), each hole is filled by a resin layer with a height of h (Region I), which is connected on a resin base plate with a thickness d_2 of λ. The density and acoustic speed of the photosensitive resin are 1120 kg·m^{-3} and 2929 m·s^{-1}, respectively [1]. The radius of the CH is $w = 2.4$ mm (~1.6λ) and Region II is filled with water. Figure 4(c) shows the variations of the transmissivity and transmitted phase shift of the acoustic plane wave through the CH with the height h of the resin layer. It is observed that, by changing h-value from 0 to 8 mm, the transmitted phase shift can change from 0 to 2π with relative high transmissivity. For example, when the h-values of the resin layer are set as 1.01, 7.67, 4.96, 2.2204, 5.626, 3.03, 3.43, and 6.79 mm, respectively, the corresponding transmitted phase shift are about 0, $\pi/4$, $\pi/2$, $3\pi/4$, π,

$5\pi/4$, $6\pi/4$, and $7\pi/4$. We have fabricated an AASP that contains 24 CHs filled with different thickness resin layer to realize the PPAV with $l = 3$ and $N = 2$.

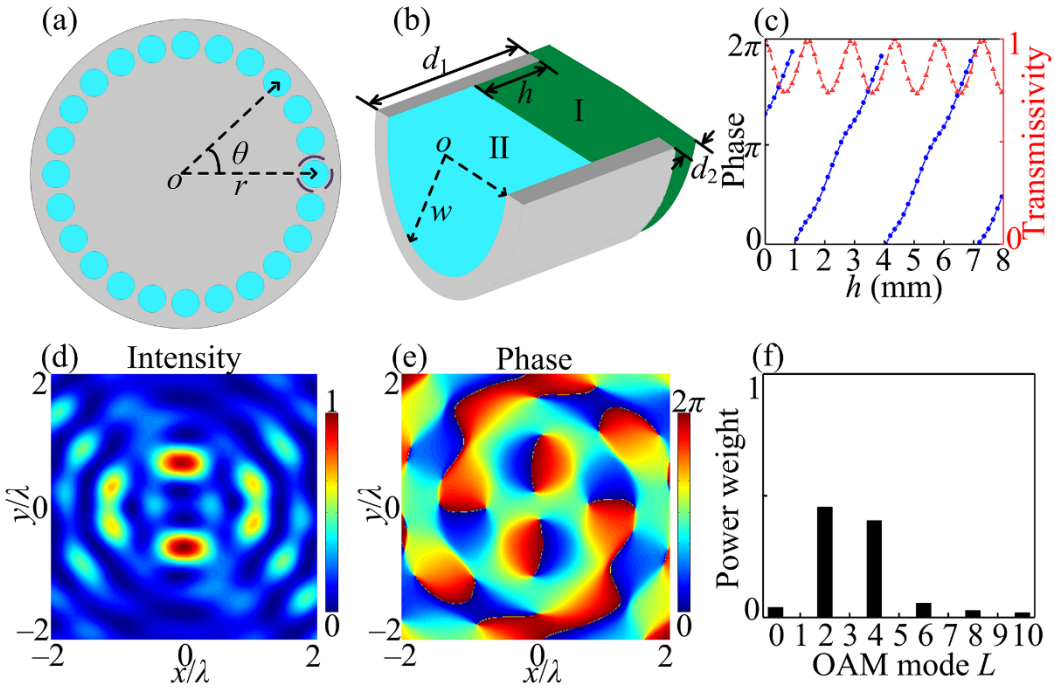

FIG. 4. (a) Schematic diagram of the acoustic artificial structure plate (AASP) for generating the PPAV with $l = 3$ and $N = 2$. (b) Three-dimensional diagram of the circular hole (CH) unit filled with a resin layer. (c) Variations of the transmissivity and phase shift of the transmitted acoustic field through one CH unit with the thickness h of the filling resin layer. (d) Normalized simulated acoustic intensity distribution, (e) phase distribution, and (f) OAM spectrum of the transmitted acoustic field through the AASP. Here, the observed plane is $z = 7\lambda$.

Figures 4(d) and 4(e) show the simulated normalized acoustic intensity distribution and phase distribution of the transmitted acoustic field through the AASP at the plane of $z = 7\lambda$, which are almost in accord with those analytical results of the PPAV with $l = 3$ and $N = 2$. In the simulated OAM spectrum shown in Fig. 4(f), the power is still mainly distributed in two OAM components of $L = 2$ (~45%) and 4 (~40%) and the sample interval of the OAM spectrum is 2.

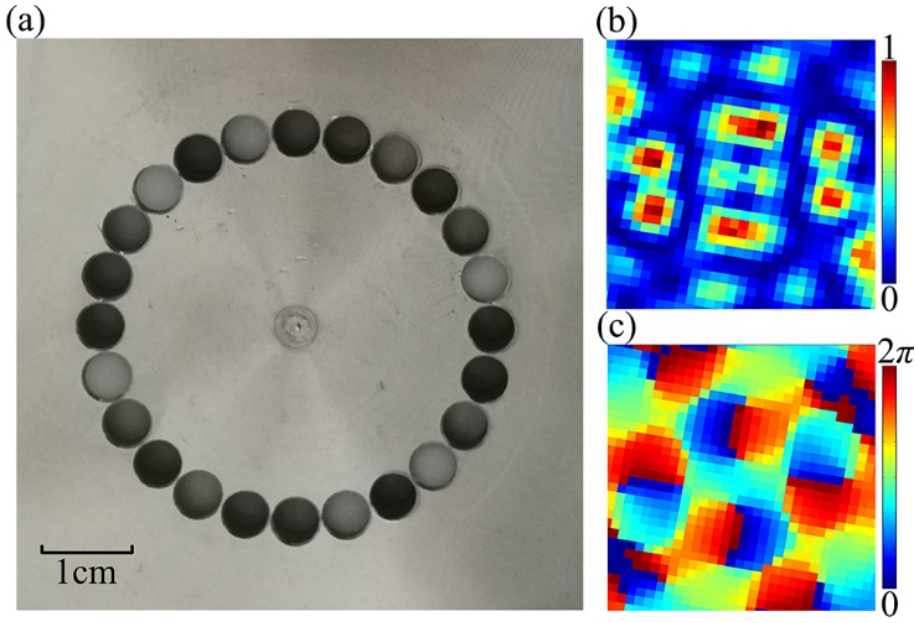

FIG. 5. (a) Photograph of the AASP sample for generating a PPAV with $l = 3$ and $N = 2$ in water. (b) Normalized measured acoustic intensity and (c) phase distributions of the PPAV with $l = 3$ and $N = 2$ at the plane of $z \approx 7\lambda$.

Based on the simulations, we further fabricated an AASP sample to experimentally realize a PPAV. Figure 5(a) shows a photograph of the AASP sample for generating a PPAV with $l = 3$ and $N = 2$ in water. The AASP substrate engraved with 24 CHs is made of stainless steel using laser engraving technology and the filling resin layer of each CH is fabricated using 3D printing technology. In the experiment, an ultrasound transducer with a central frequency of 1 MHz is placed on back of the AASP sample, which is supported by a clamp holder. A needle hydrophone (NH0500, Precision Acoustics) is used to measure the acoustic field, which was fixed on an *x*-*y*-*z* control system. Figures 5(b) and 5(c) represent the normalized measured acoustic intensity and phase distributions of the PPAV with $l = 3$ and $N = 2$ at the plane of $z \approx 7\lambda$, respectively. It is observed that two bright spots and two dark spots on *y*-axis and two dark stripes on *x*-axis in the measured acoustic intensity distributions, while four phase singularities distinctly appear in the measured phase profile. The experiment results match well with the

simulated and analytical results. Therefore, the proposed AASP can generate the PPAV experimentally.

Finally, we have proposed an acoustic encoding/decoding communication based on the OAM sample interval of the PPAV, where the OAM sample interval is chosen as an independent degree of freedom for information encoding/decoding. Here, we have introduced the binary code as a reference for the encoding/decoding communication and thus 2 PPAVs are used to represent 2 binary codes of "0" and "1". In Figs. 6(a) and 6(b), two PPAVs are set as 2 bases of B_0 and B_1 corresponding to "0" and "1" in binary representations, respectively. For the base B_0 (PPAV with $l = 3$ and $N = 2$) in Fig. 6(a), the power weights of two OAM components of $L = 2$ and 4 account for the largest proportion and the OAM sample interval N_0 is equal to 2. The PPAV with $l = 4.5$ and $N = 3$ is encoded as base B_1, as shown in Fig. 6(b). The power weights of two OAM components of $L = 3$ and 6 account for the largest proportion, and the OAM sample interval N_1 is equal to 3. Thus, the codes of "0" and "1" can be decoded by calculating "$N - 2$". Figure 6(c) represents the orthogonality matrix between 2 bases of B_0 and B_1 by means of the inner product between two acoustic pressures distributions [6]. It is found that B_0 and B_1 are orthogonal to each other, and the crosstalk between them is calculated to be less than ~–10.4 dB, which is lower than that in Refs. 4 and 6. Therefore, the orthogonal PPAVs can be used in acoustic communication system. In principle, other orthogonal PPAVs can also be used for encoding/decoding information. If we encode in quaternary, 4 PPAVs should be encoded as 4 quaternary codes of "0", "1", "2", and "3".

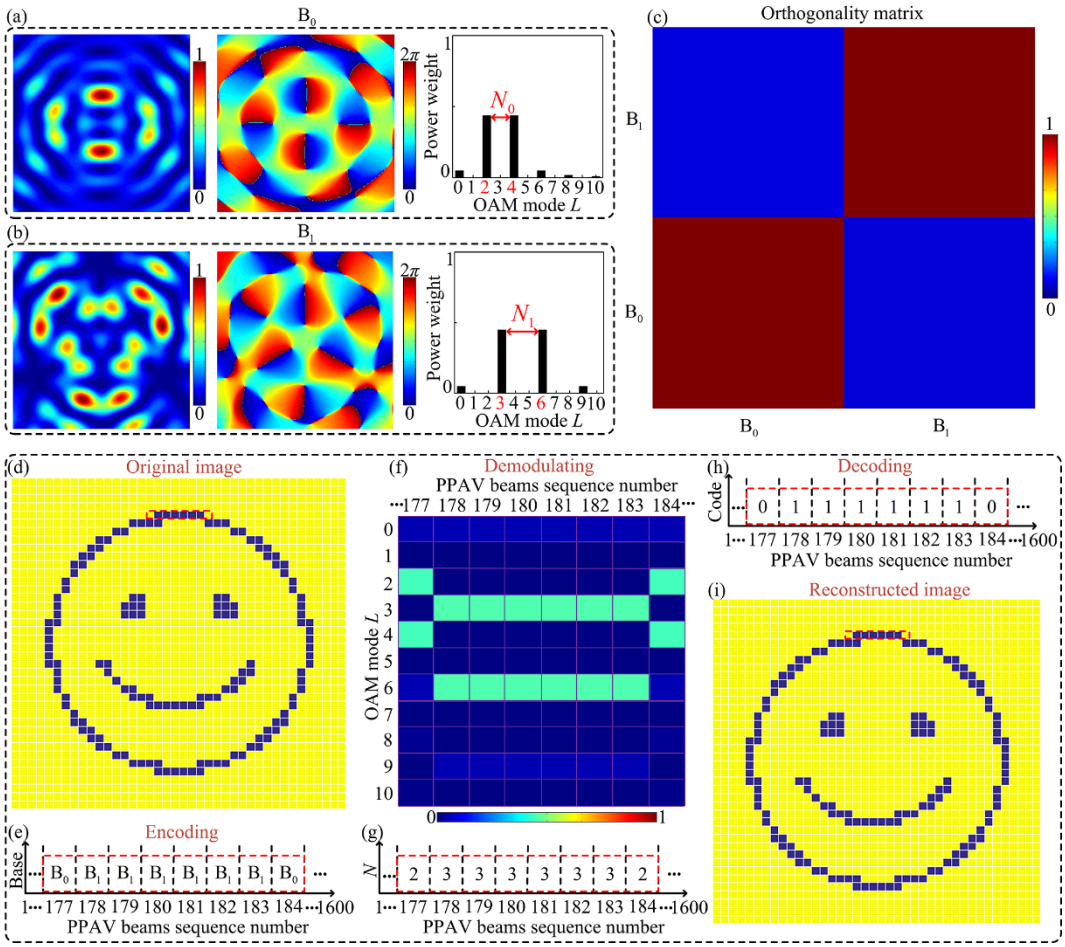

FIG. 6. Scheme for acoustic coded communication based on PPAVs. Normalized analytical acoustic intensity distributions, phase distributions, and OAM spectra of two bases of (a) "B_0" and (b) "B_1" at the plane of $z = 7\lambda$. (c) Orthogonality matrix between "B_0" and "B_1". (d) Original image of a smiling face. (e) PPAV beams sequence at the transmitter end. (f) Demodulated OAM spectra of 8 PPAVs in the sequence on the receiver side and (g) corresponding OAM sample interval N. (h) Decoded binary date stream and (i) reconstructed image.

In Fig. 6(d), a picture of a smiling face discretized into 40 × 40 pixels is used as an original image. Each pixel can be translated into a binary code of "0" or "1" according to the "yellow" or "blue" color. For example, the colors from the 177th pixel to the 184th pixel of the original image are "yellow", "blue", "blue", "blue", "blue", "blue", "blue", and "yellow", which are translated into 8 binary codes of "0", "1", "1", "1", "1", "1", "1", and "0", respectively.

Therefore, they can be encoded as a beam sequence with 8 PPAVs of "$B_0B_1B_1B_1B_1B_1B_1B_0$" at the transmitter end, as shown in Fig. 6(e). Figure 6(f) shows the demodulated OAM spectra of 8 PPAVs in the sequence on the receiver side and the corresponding OAM sample interval N is "23333332" [Fig. 6(g)]. Thus, the obtained decoded binary date stream is "01111110" according to "$N-2$" [Fig. 6(h)]. Finally, the transmitted image is reconstructed, as shown in Fig. 6(i). The OAM sample interval of the PPAV can be chosen as an independent degree of freedom for acoustic encoding/decoding communication with lower cross-talk. Moreover, it has been reported that the multi-path systems are helpful in delivering large capacity in free space [39,40]. To further demonstrate the potential of the OAM sample interval of the PPAV in acoustic communication, we additionally develop a multipath parallel communication system in the Supplement Material.

IV. CONCLUSION

We have proposed a PPAV with comb-like OAM spectrum, and the sample interval of OAM spectrum of the PPAV can be adjusted by changing the period number of the azimuthal phase. The dynamic variations of the acoustic properties of the PPAVs with increasing TC are clarified carefully. The sample interval of the components in the OAM spectrum of the PPAV is further confirmed to be the same as the period number N. Moreover, an AASP engraved with 24 filling CHs is designed to achieve the PPAVs in water. As an ultrasonic plane wave illuminates on the AASP, the transmitted phase shift of the CH unit could be flexibly and efficiently manipulated by changing the height of the resin layer filled in each hole unit, hence, the PPAV with arbitrary TC can be generated by the AASP. We have fabricated an AASP sample and experimentally confirmed the generation of the PPAV by the well-designed AASP. Finally, we have confirmed that the OAM sample interval of the PPAV can be chosen as an independent degree of freedom for acoustic encoding/decoding communication. Indeed, the inhomogeneous medium in the real underwater environment leads to the reflection and refraction of acoustic wave due to the

change in the density [41]. Zou et al. [19] experimentally placed a vortex source below the water surface, and the source was oriented upward toward the water-air boundary at the angle of 45°. It was found that the incident and reflected phase patterns are reversed. The communication performance also should be characterized by data transmission rate, spectrum efficiency, bit-error-rate, etc. These are important to explore the practical applications of AVs in real underwater environment. Therefore, more work should be put into our future experimental investigations of the transmission of PPAVs in inhomogeneous media and the effectiveness of communication.

ACKNOWLEDGEMENTS

This work was supported by the National Natural Science Foundation of China (12174197, 12074191, and 12027808) and the Postgraduate Research & Practice Innovation Program of Jiangsu Province (KYCX22_1537).

REFERENCES

[1] Q. X. Zhou, J. Zhang, X. M. Ren, Z. Xu, and X. J. Liu, Acoustic trapping of particles using a Chinese taiji lens, Ultrasonics **110**, 106262 (2021).

[2] Z. Y. Sun, Y. Shi, X. C. Sun, H. Jia, Z. K. Jin, K. Deng, and J. Yang, Underwater acoustic multiplexing communication by pentamode metasurface, J. Phys. D: Appl. Phys. **54**, 205303 (2021).

[3] Z. Y. Hong, J. Zhang, and B. W. Drinkwater, On the radiation force fields of fractional-order acoustic vortices, Europhys. Lett. **110**, 14002 (2015).

[4] C. Z. Shi, M. Dubois, Y. Wang, and X. Zhang, High-speed acoustic communication by multiplexing orbital angular momentum, Proc. Natl. Acad. Sci. U. S. A. **114**, 7250 (2017).

[5] X. Jiang, B. Liang, J. C. Cheng, and C. W. Qiu, Twisted acoustics: metasurface-enabled multiplexing and demultiplexing, Adv. Mater. **30**, 1800257 (2018).

[6] X. R. Li, Y. R. Jia, Y. C. Luo, J. Yao, and D. J. Wu, Coupled focused acoustic vortices generated by degenerated artificial plates for acoustic coded communication, Adv. Mater. Technol. **7**, 2200102 (2022).

[7] X. R. Li, Y. R. Jia, Y. C. Luo, J. Yao, and D. J. Wu, Mixed focused-acoustic-vortices generated by an artificial structure plate engraved with discrete rectangular holes Appl. Phys. Lett. **118**, 043503 (2021).

[8] Y. C. Luo, Y. R. Jia, J. Yao, D. J. Wu, and X. J. Liu, Enhanced fractional acoustic vortices by an annulus acoustic metasurface with multi-layered rings, Adv. Mater. Technol. **5**, 2000356 (2020).

[9] S. W. Fan, Y. F. Wang, L. Y. Cao, Y. F. Zhu, A. Chen, B. Vincent, B. Assouar, and Y. S. Wang, Acoustic vortices with high-order orbital angular momentum by a continuously tunable metasurface, Appl. Phys. Lett. **116**, 163504 (2020).

[10] Q. Feng, X. D. Kong, M. M. Shan, Y. F. Lin, L. Li, and T. J. Cui, Multi-orbital-angular-

momentum-mode vortex wave multiplexing and demultiplexing with shared-aperture reflective metasurfaces, Phys. Rev. Appl. **17**, 034017 (2022).

[11] J. J. Jin, X. Li, M. B. Pu, Y. H. Guo, P. Gao, M. F. Xu, Z. J. Zhang, X. G. Luo, Angular-multiplexed multichannel optical vortex arrays generators based on geometric metasurface, iScience **24**, 102107 (2021).

[12] L. J. Yang, S. Sun, and W. E. I. Sha, Manipulation of orbital angular momentum spectrum using shape-tailored metasurfaces, Adv. Opt. Mater. **9**, 2001711 (2021).

[13] V. V. Kotlyar, and A. A. Kovalev, Optical vortex beams with a symmetric and almost symmetric OAM spectrum, J. Opt. Soc. Am. A. **38**, 1276 (2021).

[14] H. P. Zhou, J. J. Li, K. Guo, and Z. Y. Guo, Generation of acoustic vortex beams with designed Fermat's spiral diffraction grating, J. Acoust. Soc. Am. **146**, 4237 (2019).

[15] M. P. J. Lavery, Vortex instability in turbulent free-space propagation, New J. Phys. **20**, 043023 (2018).

[16] M. Li, Orbital-angular-momentum multiplexing optical wireless communications with adaptive modes adjustment in internet-of-things networks, IEEE Internet Things J. **6**, 6134 (2019).

[17] K. Wu, J. J. Liu, Y. J. Ding, W. Wang, B. Liang, J. C. Cheng, Metamaterial-based real-time communication with high information density by multipath twisting of acoustic wave, Nat. Commun. **13**, 5171 (2022).

[18] J. J. Liu, Y. J. Ding, K. Wu, B. Liang, J. C. Cheng, Compact acoustic monolayered metadecoder for efficient and flexible orbital angular momentum demultiplexing, Appl. Phys. Lett. **119**, 213502 (2021).

[19] Z. G. Zou, R. Lirette, and L. K. Zhang, Orbital angular momentum reversal and asymmetry in acoustic vortex beam reflection, Phys. Rev. Lett. **125,** 074301 (2020).

[20] M. Li, M. Cvijetic, Y. Takashima, and Z. Yu, Evaluation of channel capacities of OAM

based FSO link with real-time wavefront correction by adaptive optics, Opt. Express, **22**, 31337 (2014).

[21] M. Li, Z. Yu, and M. Cvijetic, Influence of atmospheric turbulence on OAM-based FSO system with use of realistic link model, Opt. Commun. **364**, 50 (2016).

[22] Y. Yan, G. D. Xie, M. P. J. Lavery, H. Huang, N. Ahmed, C. J. Bao, Y. X. Ren, Y. W. Cao, L. Li, Z. Zhao, A. F. Molisch, M. Tur, M. J. Padgett, and A. E. Willner, High-capacity millimetre-wave communications with orbital angular momentum multiplexing, Nat. Commun. **5**, 4876 (2014).

[23] M. Zahidy, Y. X. Liu, D. Cozzolino, Y. H. Ding, T. Morioka, L. K. Oxenlowe, D. Bacco, Photonic integrated chip enabling orbital angular momentum multiplexing for quantum communication, Nanophotonics, **11**, 821 (2021).

[24] M. Barbuto, M. A. Miri, A. Alù, F. Bilotti, and A. Toscano, Exploiting the topological robustness of composite vortices in radiation systems, Prog. Electromag. Res. **162**, 39 (2018).

[25] Y. J. Yang, Q. Zhao, L. L. Liu, Y. D. Liu, C. Rosales-Guzmán, C. W. Qiu, Manipulation of orbital-angular-momentum spectrum using pinhole plates, Phys. Rev. Appl. **12**, 064007 (2019).

[26] Z. Qiao, Z. Y. Wan, G. Q. Xie, J. Wang, L. J. Qian, and D. Y. Fan, Multi-vortex laser enabling spatial and temporal encoding, PhotoniX, **1**, 13 (2020).

[27] H. X. Ma, X. Z. Li, H. Zhong, J. Tang, H. H. Li, M. M. Tang, J. G. Wang, and Y. J. Cai, Optical vortex shaping via a phase jump factor, Opt. Lett. **44**, 1379 (2019).

[28] J. T. Hu, Y. P. Tai, L. H. Zhu, Z. X. Long, M. M. Tang, H. H. Li, X. Z. Li, and Y. J. Cai, Optical vortex with multi-fractional orders, Appl. Phys. Lett. **116**, 201107 (2020).

[29] H. Q. Liu, C. X. Teng, H. Y. Yang, H. G. Deng, R. H. Xu, S. J. Deng, M. Chen, and L. B. Yuan, Proposed phase plate for superimposed orbital angular momentum state generation,

Opt. Express **26**, 14792 (2018).

[30] Z. Sun, H. Z. Guo, and I. F. Akyildiz, High-data-rate long-range underwater communications via acoustic reconfigurable intelligent surfaces, IEEE Communications Magazine, **60**, 96 (2022).

[31] P. Q. Li, Z. L. Li, W. Zhou, S. W. Wang, L. Meng, Y. G. Peng, Z. Chen, H. R. Zheng, and X. F. Zhu, Generating multistructured ultrasound via bioinspired metaskin patterning for low-threshold and contactless control of living organisms, Adv. Funct. Mater. **32**, 2203109 (2022).

[32] L. Tong, Z. Xiong, Y. X. Shen, Y. G. Peng, X. Y. Huang, L. Ye, M. Tang, F. Y. Cai, H. R. Zheng, J. B. Xu, G. J. Cheng, and X. F. Zhu, An acoustic meta-skin insulator, Adv. Mater. **32**, 2002251 (2020).

[33] Y. X. Shen, Y. G. Peng, F. Y. Cai, K. Huang, D. G. Zhao, C. W. Qiu, H. R. Zheng, and X. F. Zhu, Ultrasonic super-oscillation wave-packets with an acoustic meta-lens, Nat. Commun. **10**, 3411 (2019).

[34] X. Jiang, J. J. Zhao, S. L. Liu, B. Liang, A. Y. Zou, J. Yang, C. W. Qiu, and J. C. Cheng, Broadband and stable acoustic vortex emitter with multi-arm coiling slits, Appl. Phys. Lett. **108**, 203501 (2016).

[35] X. M. Ren, Q. X. Zhou, Z. Xu, and X. J. Liu, Particle trapping in arbitrary trajectories using first-order Bessel-like acoustic beams, Phys. Rev. Appl. **15**, 054041 (2021).

[36] Y. J. Yang, G. Thirunavukkarasu, M. Babiker, and J. Yuan, Orbital-angular-momentum mode selection by rotationally symmetric superposition of chiral states with application to electron vortex beams, Phys. Rev. Lett. **119**, 094802 (2017).

[37] Y. R. Jia, W. Q. Ji, D. J. Wu, and X. J. Liu, Metasurface-enabled airborne fractional acoustic vortex emitter, Appl. Phys. Lett. **113**, 173502 (2018).

[38] N. Zhang, J. A. Davis, I. Moreno, J. Lin, K. J. Moh, D. M. Cottrell, and X. C. Yuan, Analysis

of fractional vortex beams using a vortex grating spectrum analyzer, Appl. Opt. **49**, 2456 (2010).

[39] Y. X. Ren, Z. Wang, G. D. Xie, L. Li, Y. W. Cao, C. Liu, P. C. Liao, Y. Yan, N. Ahmed, Z. Zhao, A. Willner, N. Ashrafi, S. Ashrafi, R. D. Linquist, R. Bock, M. Tur, A. F. Molisch, and A. E. Willner, Free-space optical communications using orbital-angular-momentum multiplexing combined with mimo-based spatial multiplexing, Opt. Lett. **40**, 4210 (2015).

[40] Q. B. Zhu, T. Jiang, D. M. Qu, D. Chen, and N. R. Zhou, Radio Vortex–multiple-input multiple-output communication systems with high capacity, IEEE Access **3**, 2456 (2015).

[41] H. Kaushal, and G. Kaddoum, Underwater optical wireless communication, IEEE Access **4**, 1518 (2016).

[42] See Supplementary Material for the propagation properties of the PPAV, the acoustic intensity and phase distributions produced by the first and second phase periods of the PPAV with $l = 3$ and $N = 2$, the detailed evolution process of the PPAV, PPAVs with same TC l but varying period number N, and a multipath parallel acoustic encoding/decoding communication system for sending letters.

FIGURE CAPTIONS:

FIG. 1. (a) Schematic diagram of an original analytical model for a PPAV with TC $l = 3$ and period number $N = 2$. (b) Dependence of the phase ψ_{PPAV} of the PPAV with $l = 3$ and $N = 2$ on the azimuthal angle θ. (c) Normalized analytical acoustic intensity and (d) phase distributions of the PPAV with $l = 3$ and $N = 2$. (e) Corresponding OAM spectrum of the PPAV.

FIG. 2. (a1)-(a5) Dependencies of the phase ψ_{PPAV} of the PPAVs with $l = 2$, 2.5, 3, 3.5, and 4 on the azimuthal angle θ. Here, the period number N is fixed at 2. (b1)-(b5) Normalized analytical acoustic intensity and (c1)-(c5) phase distributions of the PPAVs with $l = 2$, 2.5, 3, 3.5, and 4. Here, the observed plane is $z = 7\lambda$. (d1)-(d5) Corresponding OAM spectra of the PPAVs.

FIG. 3. Variations of the phase ψ_{PPAV} of the PPAVs with (a1) $l = 1.5$ and $N = 1$, (a2) $l = 3$ and $N = 2$, (a3) $l = 4.5$ and $N = 3$, and (a4) $l = 6$ and $N = 4$ with θ. (b1)-(b4) Normalized analytical acoustic intensity and (c1)-(c4) phase distributions of the PPAVs with $l = 1.5$ and $N = 1$, $l = 3$ and $N = 2$, $l = 4.5$ and $N = 3$, and $l = 6$ and $N = 4$. Here, the observed plane is $z = 7\lambda$. (d1)-(d4) Corresponding OAM spectra of the PPAVs.

FIG. 4. (a) Schematic diagram of the acoustic artificial structure plate (AASP) for generating the PPAV with $l = 3$ and $N = 2$. (b) Three-dimensional diagram of the circular hole (CH) unit filled with a resin layer. (c) Variations of the transmissivity and phase shift of the transmitted acoustic field through one CH unit with the thickness h of the filling resin layer. (d) Normalized simulated acoustic intensity distribution, (e) phase distribution, and (f) OAM spectrum of the transmitted acoustic field through the AASP. Here, the observed plane is $z = 7\lambda$.

FIG. 5. (a) Photograph of the AASP sample for generating a PPAV with $l = 3$ and $N = 2$ in water. (b) Normalized measured acoustic intensity and (c) phase distributions of the PPAV with $l = 3$ and $N = 2$ at the plane of $z \approx 7\lambda$.

FIG. 6. Scheme for acoustic coded communication based on PPAVs. Normalized analytical acoustic intensity distributions, phase distributions, and OAM spectra of two bases of (a) "B_0" and (b) "B_1" at the plane of $z = 7\lambda$. (c) Orthogonality matrix between "B_0" and "B_1". (d) Original image of a smiling face. (e) PPAV beams sequence at the transmitter end. (f) Demodulated OAM spectra of 8 PPAVs in the sequence on the receiver side and (g) corresponding OAM sample interval N. (h) Decoded binary date stream and (i) reconstructed image.

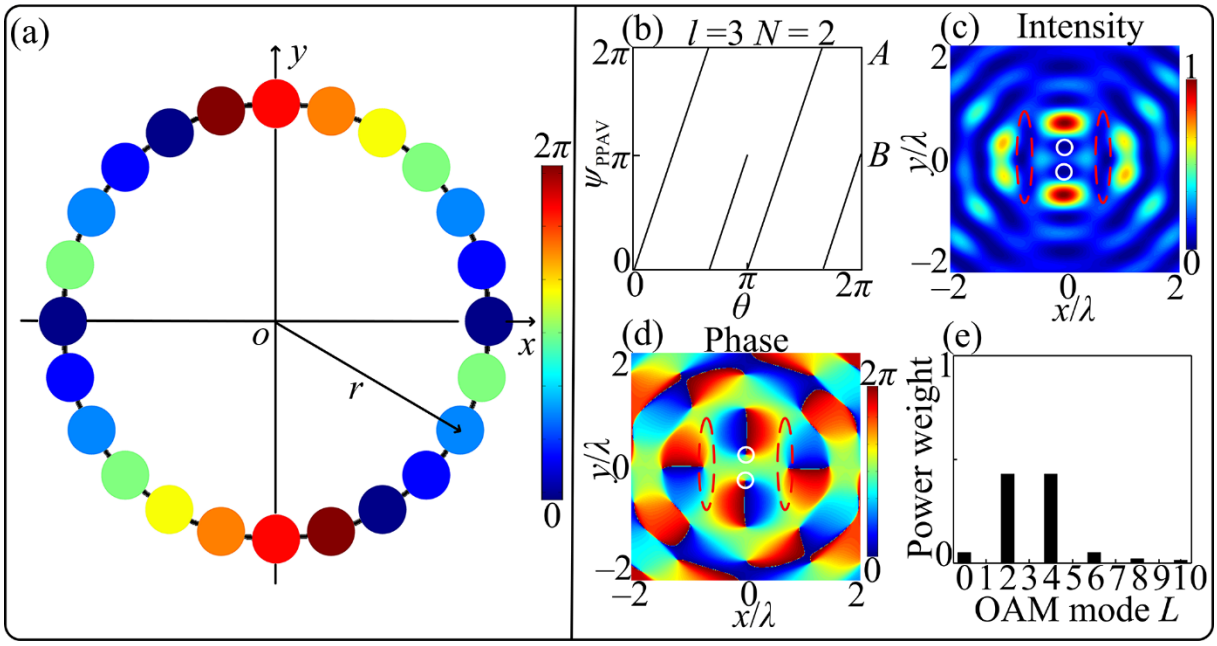

Figure 1: X. R. Li *et al.*

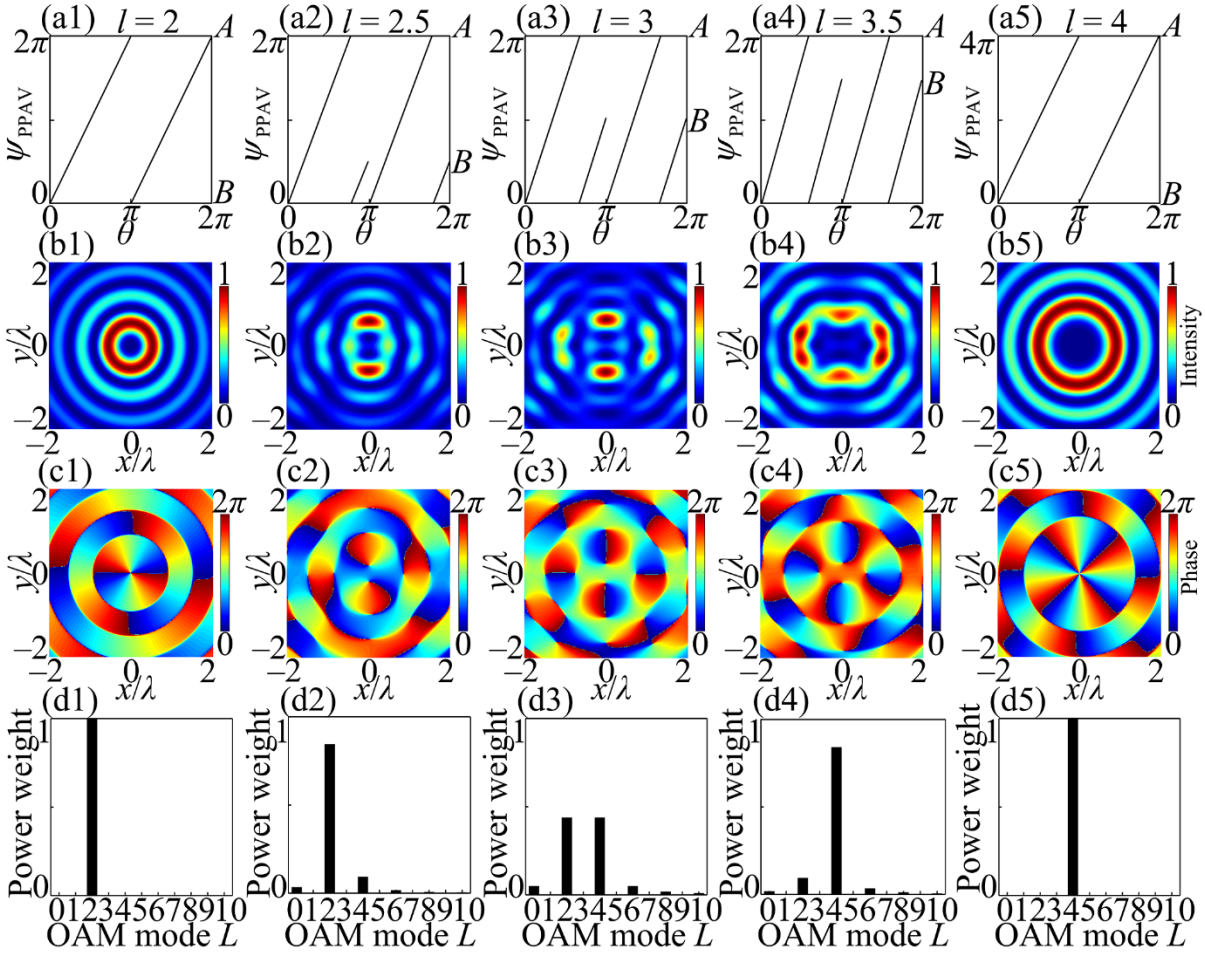

Figure 2: X. R. Li *et al.*

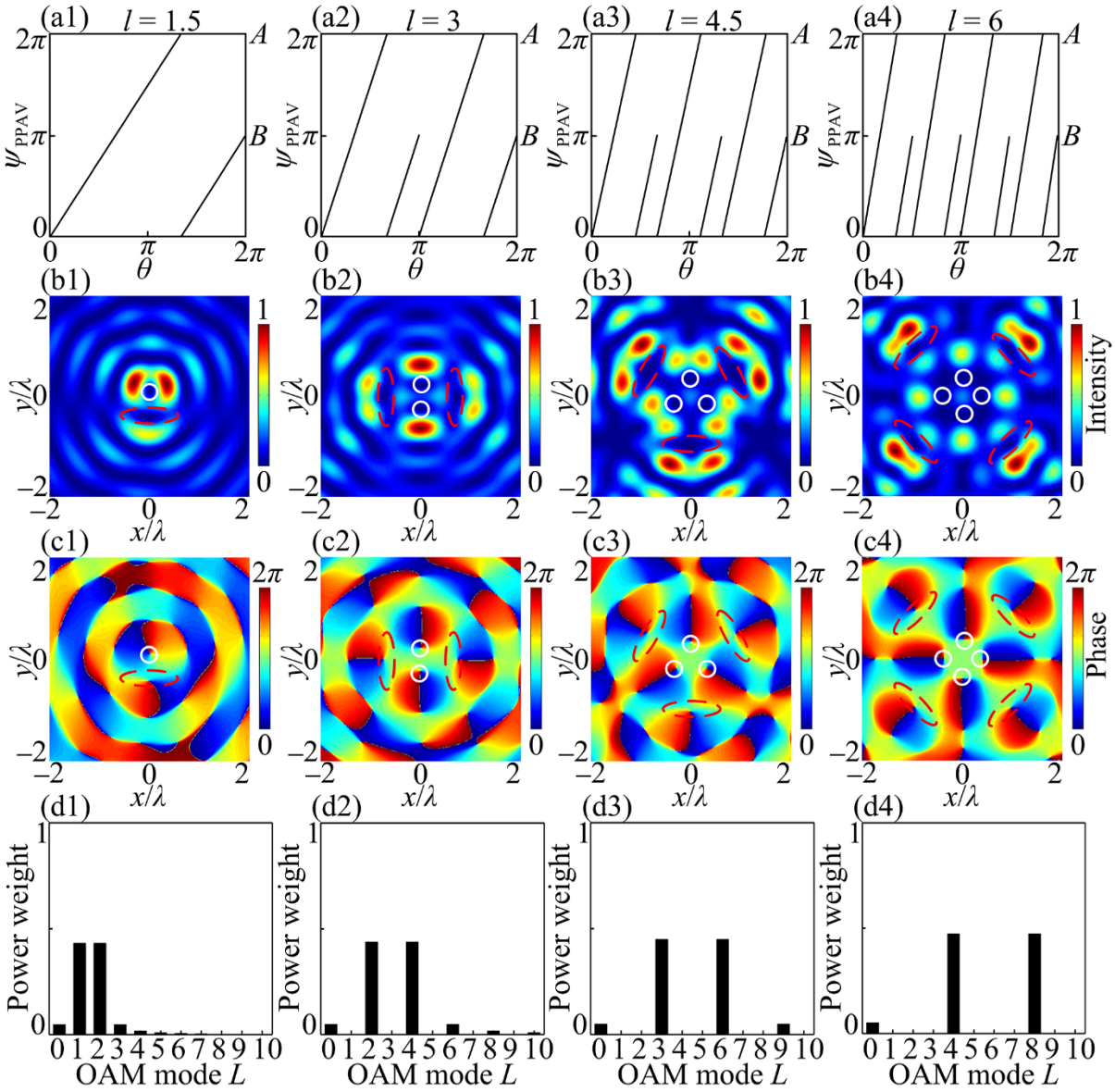

Figure 3: X. R. Li *et al.*

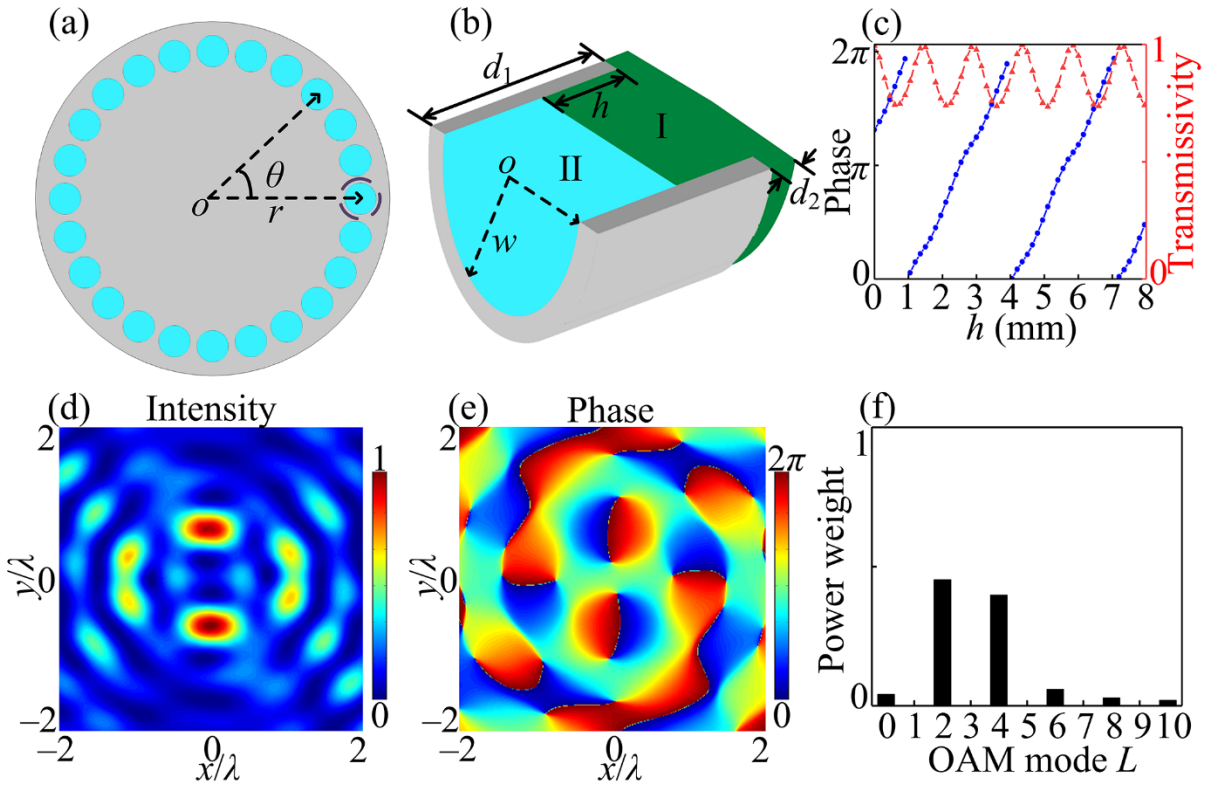

Figure 4: X. R. Li *et al.*

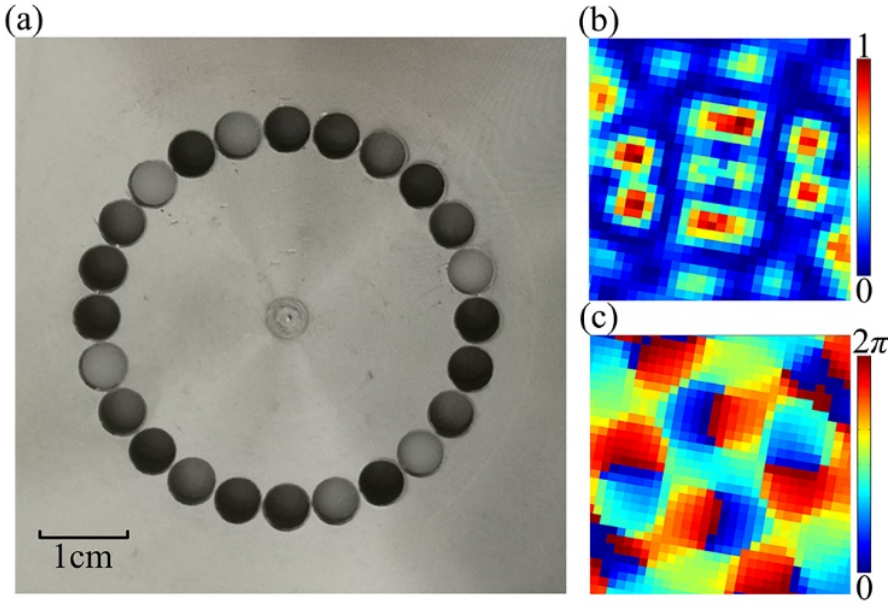

Figure 5: X. R. Li *et al.*

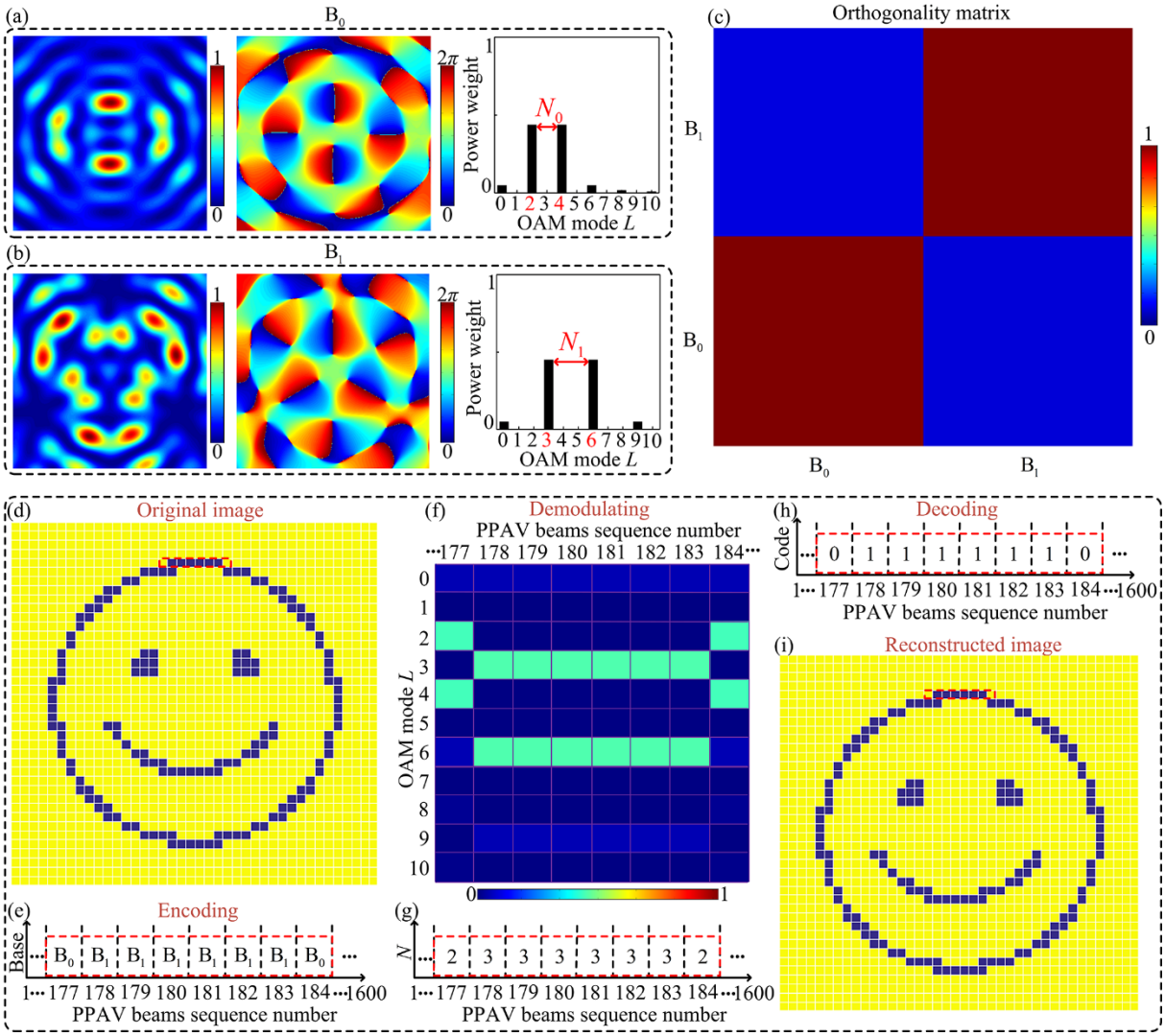

Figure 6: X. R. Li *et al.*